

Modeling high-peak-power few-cycle field waveform generation by optical parametric amplification in the long-wavelength infrared

A.A. VORONIN,^{1,2} A.A. LANIN,^{1,2} AND A.M. ZHELTIKOV^{1,2,3*}

¹Physics Department, International Laser Center, M. V. Lomonosov Moscow State University, Moscow 119992, Russia

²Russian Quantum Center, 143025 Skolkovo, Moscow Region, Russia

³Department of Physics and Astronomy, Texas A&M University, 77843 College Station TX, USA

*zheltikov@physics.msu.ru

Abstract: Extended coupled-wave analysis of optical parametric chirped-pulse amplification (OPCPA) reveals regimes whereby high-peak-power few-cycle pulses can be generated in the long-wavelength infrared (LWIR) spectral range. Broadband OPCPA in suitable nonlinear crystals pumped at around 2 μm and seeded either through the signal or the idler input is shown to enable the generation of high-power field waveforms with pulse widths shorter than two field cycles within the entire LWIR range.

© 2016 Optical Society of America

OCIS codes: (320.7090) Ultrafast lasers; (190.4970) Parametric oscillators and amplifiers

References and links

1. X. Franz, Kärtner, *Few-Cycle Laser Pulse Generation and Its Applications* (Springer, 2004).
2. P. B. Corkum and F. Krausz, “Attosecond science,” *Nat. Phys.* **3**(6), 381–387 (2007).
3. P. Agostini and L. F. DiMauro, “Atoms in high intensity mid-infrared pulses,” *Contemp. Phys.* **49**(3), 179–197 (2008).
4. P. Colosimo, G. Doumy, C. I. Blaga, J. Wheeler, C. Hauri, F. Catoire, J. Tate, R. Chirla, A. M. March, G. G. Paulus, H. G. Muller, P. Agostini, and L. F. DiMauro, “Scaling strong-field interactions towards the classical limit,” *Nat. Phys.* **4**(5), 386–389 (2008).
5. G. Andriukaitis, T. Balčiūnas, S. Ališauskas, A. Pugžlys, A. Baltuška, T. Popmintchev, M.-C. Chen, M. M. Murnane, and H. C. Kapteyn, “90 GW peak power few-cycle mid-infrared pulses from an optical parametric amplifier,” *Opt. Lett.* **36**(15), 2755–2757 (2011).
6. T. Popmintchev, M.-C. Chen, D. Popmintchev, P. Arpin, S. Brown, S. Ališauskas, G. Andriukaitis, T. Balčiūnas, O. D. Mücke, A. Pugžlys, A. Baltuška, B. Shim, S. E. Schrauth, A. Gaeta, C. Hernández-García, L. Plaja, A. Becker, A. Jaron-Becker, M. M. Murnane, and H. C. Kapteyn, “Bright coherent ultrahigh harmonics in the keV X-ray regime from mid-infrared femtosecond lasers,” *Science* **336**(6086), 1287–1291 (2012).
7. A. V. Mitrofanov, A. A. Voronin, D. A. Sidorov-Biryukov, A. Pugžlys, E. A. Stepanov, G. Andriukaitis, T. Flöry, S. Ališauskas, A. B. Fedotov, A. Baltuška, and A. M. Zheltikov, “Mid-infrared laser filaments in the atmosphere,” *Sci. Rep.* **5**, 8368 (2015).
8. A. V. Mitrofanov, A. A. Voronin, D. A. Sidorov-Biryukov, S. I. Mitryukovsky, A. B. Fedotov, E. E. Serebryannikov, D. V. Meshchankin, V. Shumakova, S. Ališauskas, A. Pugžlys, V. Ya. Panchenko, A. Baltuška, and A. M. Zheltikov, “Subterawatt few-cycle mid-infrared pulses from a single filament,” *Optica* **3**(3), 299–302 (2016).
9. J. Weisshaupt, V. Juvé, M. Holtz, S. Ku, M. Woerner, T. Elsaesser, S. Ališauskas, A. Pugžlys, and A. Baltuška, “High-brightness table-top hard X-ray source driven by sub-100-femtosecond mid-infrared pulses,” *Nat. Photonics* **8**(12), 927–930 (2014).
10. D. Kartashov, S. Ališauskas, A. Pugžlys, A. Voronin, A. Zheltikov, M. Petrarca, P. Béjot, J. Kasparian, J.-P. Wolf, and A. Baltuška, “White light generation over three octaves by femtosecond filament at 3.9 μm in argon,” *Opt. Lett.* **37**(16), 3456–3458 (2012).
11. A. V. Mitrofanov, A. A. Voronin, S. I. Mitryukovskiy, D. A. Sidorov-Biryukov, A. Pugžlys, G. Andriukaitis, T. Flöry, E. A. Stepanov, A. B. Fedotov, A. Baltuška, and A. M. Zheltikov, “Mid-infrared-to-mid-ultraviolet supercontinuum enhanced by third-to-fifteenth odd harmonics,” *Opt. Lett.* **40**(9), 2068–2071 (2015).
12. D. Kartashov, S. Ališauskas, G. Andriukaitis, A. Pugžlys, M. Shneider, A. Zheltikov, S. L. Chin, and A. Baltuška, “Free-space nitrogen gas laser driven by a femtosecond filament,” *Phys. Rev. A* **86**(3), 033831 (2012).
13. D. Kartashov, S. Ališauskas, A. Pugžlys, A. A. Voronin, A. M. Zheltikov, and A. Baltuška, “Third- and fifth-harmonic generation by mid-infrared ultrashort pulses: beyond the fifth-order nonlinearity,” *Opt. Lett.* **37**(12), 2268–2270 (2012).

14. E. E. Serebryannikov and A. M. Zheltikov, "Quantum and semiclassical physics behind ultrafast optical nonlinearity in the midinfrared: the role of ionization dynamics within the field half cycle," *Phys. Rev. Lett.* **113**(4), 043901 (2014).
15. D. Sanchez, M. Hemmer, M. Baudisch, S. L. Cousin, K. Zawilski, P. Schunemann, O. Chalus, C. Simon-Boisson, and J. Biegert, "7 μm , ultrafast, sub-millijoule-level mid-infrared optical parametric chirped pulse amplifier pumped at 2 μm ," *Optica* **3**(2), 147–150 (2016).
16. J. M. Chalmers and P. R. Griffiths, *Handbook of Vibrational Spectroscopy* (Wiley, 2002).
17. A. Krier, *Mid-Infrared Semiconductor Optoelectronics* (Springer-Verlag, 2006), p. 118.
18. A. Schliesser, N. Picqué, and T. W. Hänsch, "Mid-infrared frequency combs," *Nat. Photonics* **6**(7), 440–449 (2012).
19. M. Jahjah, W. Jiang, N. P. Sanchez, W. Ren, P. Patimisco, V. Spagnolo, S. C. Herndon, R. J. Griffin, and F. K. Tittel, "Atmospheric CH₄ and N₂O measurements near Greater Houston area landfills using a QCL-based QEPAS sensor system during DISCOVER-AQ 2013," *Opt. Lett.* **39**(4), 957–960 (2014).
20. S. Liakat, K. A. Bors, L. Xu, C. M. Woods, J. Doyle, and C. F. Gmachl, "Noninvasive in vivo glucose sensing on human subjects using mid-infrared light," *Biomed. Opt. Express* **5**(7), 2397–2404 (2014).
21. R. H. Wilson and H. S. Tapp, "Mid-infrared spectroscopy for food analysis: recent new applications and relevant developments in sample presentation methods," *TrAC Trends Analyt. Chem.* **18**(2), 85–93 (1999).
22. A. A. Voronin, V. M. Gordienko, V. T. Platonenko, V. Y. Panchenko, and A. M. Zheltikov, "Ionization-assisted guided-wave pulse compression to extreme peak powers and single-cycle pulse widths in the mid-infrared," *Opt. Lett.* **35**(21), 3640–3642 (2010).
23. J. J. Pigeon, S. Y. Tochitsky, and C. Joshi, "High-power, mid-infrared, picosecond pulses generated by compression of a CO₂ laser beat-wave in GaAs," *Opt. Lett.* **40**(24), 5730–5733 (2015).
24. V. Petrov, "Frequency down-conversion of solid-state laser sources to the mid-infrared spectral range using non-oxide nonlinear crystals," *Prog. Quantum Electron.* **42**, 1–106 (2015).
25. A. A. Lanin, A. A. Voronin, E. A. Stepanov, A. B. Fedotov, and A. M. Zheltikov, "Multioctave, 3–18 μm sub-two-cycle supercontinua from self-compressing, self-focusing soliton transients in a solid," *Opt. Lett.* **40**(6), 974–977 (2015).
26. K. L. Vodopyanov, V. G. Voevodin, A. I. Gribenyukov, and L. A. Kulevskii, "High-efficiency picosecond parametric superradiance emitted by a ZnGeP₂ crystal in the 5–6.3 μm range," *Sov. J. Quantum Electron.* **17**(9), 1159–1161 (1987).
27. R. D. Peterson, K. L. Schepler, J. L. Brown, and P. G. Schunemann, "Damage properties of ZnGeP₂ at 2 μm ," *J. Opt. Soc. Am. B* **12**(11), 2142–2146 (1995).
28. K. T. Zawilski, P. G. Schunemann, S. D. Setzler, and T. M. Pollak, "Large aperture single crystal ZnGeP₂ for high-energy applications," *J. Cryst. Growth* **310**(7–9), 1891–1896 (2008).
29. X. Zhao, S. Zhu, B. Zhao, B. Chen, Z. He, R. Wang, H. Yang, Y. Sun, and J. Cheng, "Growth and characterization of ZnGeP₂ single crystals by the modified Bridgman method," *J. Cryst. Growth* **311**(1), 190–193 (2008).
30. K. L. Vodopyanov, "Parametric generation of tunable infrared radiation in ZnGeP₂ and GaSe pumped at 3 μm ," *J. Opt. Soc. Am. B* **10**(9), 1723–1729 (1993).
31. G. B. Abdullaev, L. A. Kulevskii, A. M. Prokhorov, A. D. Savel'Ev, E. Y. Salaev, and V. V. Smirnov, "GaSe, a new effective material for nonlinear optics," *Sov. J. Exp. Theor. Phys. Lett.* **16**, 90–92 (1972).
32. N. B. Singh, D. R. Suhre, V. Balakrishna, M. Marable, R. Meyer, N. Ferneliuss, F. K. Hopkins, and D. Zelmon, "Far-infrared conversion materials: gallium selenide for far-infrared conversion applications," *Prog. Cryst. Growth Charact. Mater.* **37**(1), 47–102 (1998).
33. K. Kato, F. Tanno, and N. Umemura, "Sellmeier and thermo-optic dispersion formulas for GaSe (Revisited)," *Appl. Opt.* **52**(11), 2325–2328 (2013).
34. G. Boyd, H. Kasper, J. McFee, and F. Storz, "Linear and nonlinear optical properties of some ternary selenides," *IEEE J. Quantum Electron.* **8**(12), 900–908 (1972).
35. N. P. Barnes, D. J. Gettemy, J. R. Hietanen, and R. A. Lannini, "Parametric amplification in AgGaSe₂," *Appl. Opt.* **28**(23), 5162–5168 (1989).
36. J. M. Dudley, G. Genty, and S. Coen, "Supercontinuum generation in photonic crystal fiber," *Rev. Mod. Phys.* **78**(4), 1135–1184 (2006).
37. A. M. Zheltikov, "Let there be white light: supercontinuum generation by ultrashort laser pulses," *Phys. Uspekhi* **49**(6), 605–628 (2006).
38. M. Hemmer, D. Sánchez, M. Jelínek, V. Smirnov, H. Jelinkova, V. Kubeček, and J. Biegert, "2- μm wavelength, high-energy Ho:YLF chirped-pulse amplifier for mid-infrared OPCPA," *Opt. Lett.* **40**(4), 451–454 (2015).
39. P. Malevich, G. Andriukaitis, T. Flöry, A. J. Verhoef, A. Fernández, S. Ališauskas, A. Pugžlys, A. Baltuška, L. H. Tan, C. F. Chua, and P. B. Phua, "High energy and average power femtosecond laser for driving mid-infrared optical parametric amplifiers," *Opt. Lett.* **38**(15), 2746–2749 (2013).
40. P. Malevich, T. Kanai, H. Hoogland, R. Holzwarth, A. Baltuška, and A. Pugžlys, "Broadband mid-infrared pulses from potassium titanyl arsenate/zinc germanium phosphate optical parametric amplifier pumped by Tm, Ho-fiber-seeded Ho:YAG chirped-pulse amplifier," *Opt. Lett.* **41**(5), 930–933 (2016).
41. P. Kroetz, A. Ruehl, G. Chatterjee, A.-L. Calendron, K. Murari, H. Cankaya, P. Li, F. X. Kärtner, I. Hartl, and R. J. Miller, "Overcoming bifurcation instability in high-repetition-rate Ho:YLF regenerative amplifiers," *Opt. Lett.* **40**(23), 5427–5430 (2015).

42. K. Murari, H. Cankaya, P. Kroetz, G. Cirmi, P. Li, A. Ruehl, I. Hartl, and F. X. Kärtner, "Intracavity gain shaping in millijoule-level, high gain Ho:YLF regenerative amplifiers," *Opt. Lett.* **41**(6), 1114–1117 (2016).
43. L. von Grafenstein, M. Bock, G. Steinmeyer, U. Griebner, and T. Elsaesser, "Taming chaos: 16 mJ picosecond Ho: YLF regenerative amplifier with 0.7 kHz repetition rate," *Laser Photonics Rev.* **10**(1), 123–130 (2016).
44. H. Fonnum, E. Lippert, and M. W. Haakestad, "550 mJ Q-switched cryogenic Ho:YLF oscillator pumped with a 100 W Tm: fiber laser," *Opt. Lett.* **38**(11), 1884–1886 (2013).
45. L. Wang, X. Cai, J. Yang, X. Wu, H. Jiang, and J. Wang, "520 mJ langasite electro-optically Q-switched Cr, Tm, Ho:YAG laser," *Opt. Lett.* **37**(11), 1986–1988 (2012).
46. Y. R. Shen, *Principles of Nonlinear Optics* (Wiley-Interscience, 1984).
47. R. Baumgartner and R. Byer, "Optical Parametrical Amplification," *IEEE J. Quantum Electron.* **15**(6), 432–444 (1979).
48. J. M. Manley and H. E. Rowe, "Some general properties of nonlinear elements: Pt 1 - General energy relations," *Proc. IRE* **44**(7), 904–913 (1956).
49. A. Harasaki and K. Kato, "New data on the nonlinear optical constant, phase-matching, and optical damage of AgGaS₂," *Jpn. J. Appl. Phys.* **36**(2 Part 1), 700–703 (1997).
50. B. C. Ziegler and K. L. Schepler, "Transmission and damage-threshold measurements in AgGaSe₂ at 2.1 μm," *Appl. Opt.* **30**(34), 5077–5080 (1991).
51. Y. Ni, H. Wu, C. Huang, M. Mao, Z. Wang, and X. Cheng, "Growth and quality of gallium selenide (GaSe) crystals," *J. Cryst. Growth* **381**, 10–14 (2013).

1. Introduction

Technologies enabling the generation of electromagnetic field waveforms as short as a few field cycles are on the cutting edge of modern optical science [1]. Such waveforms offer unique tools to probe and control extremely fast processes in a broad variety of physical, chemical, and biological systems. Ultrafast photonics provides powerful and yet elegant means to generate few-cycle waveforms in the visible, near-infrared, terahertz, and x-ray ranges [2]. The past few years have witnessed an impressive progress toward extending these approaches to the mid-infrared [3,4], where few-cycle field waveform generation has always been considered a challenge. Implemented at the very heart of the mid-IR range, at a carrier wavelength of 4 μm [5–7], optical parametric chirped pulse amplification (OPCPA) now enables the generation of few-cycle mid-IR field waveforms with peak powers up to the subterawatt level [8], opening new horizons in x-ray generation [6,9], attosecond waveform synthesis [6], laser filamentation [10,11], and remote sensing of the atmosphere [12]. Experiments performed with these sources reveal unique regimes of laser–matter interactions [13] along with unexpected optical properties of materials in the mid-IR [14].

With short-pulse OPCPA recently extended to carrier wavelengths as long as 7 μm, through a clever combination of a 2-μm pump, fiber-laser-pumped seed based on difference-frequency generation (DFG), and OPCPA in a ZGP crystal [15], the expansion of ultrafast photonics into the mid-infrared is largely complete. Its immediate neighbor, the long-wavelength infrared (LWIR) range, however, is still a *hic sunt dracones* land. Stretching from 8 to 15 μm, this spectral region is of utmost significance for molecular vibrational spectroscopy [16], semiconductor optoelectronics [17], frequency-comb technologies [18], trace-gas detection [19], biomedical diagnostics [20], and food analysis [21].

Over many decades, CO₂ lasers have dominated the landscape of optical science in this wavelength range. Although they still offer a powerful and versatile tool for numerous applications, CO₂ laser technologies are not immediately compatible with few-cycle waveform photonics as the gain band they provide is too narrow to support few-cycle laser pulses. As a means to address this problem, pulse compression approaches using gas-filled hollow fibers [22] and laser-induced filamentation [23] are being extended to the LWIR range. As an alternative, several suitable nonlinear-optical materials have been shown to enable efficient generation of widely tunable LWIR radiation through optical parametric amplification (OPA), or, for that matter, difference-frequency generation (DFG), allowing the creation of compact all-solid sources of ultrashort pulses in the LWIR [24,25]. The key question to address now is whether and how these technologies could be extended to enable the generation of few-cycle LWIR pulses at the level of peak powers already attainable in the mid-IR. This question is the main focus of the study presented in this paper.

2. Broadband OPCPA strategies

Three nonlinear crystals are examined in this work as promising media for OPCPA in the LWIR. The ZnGeP₂ (ZGP) crystal [26–28] is, perhaps, the most intensely studied nonlinear crystal for parametric wavelength conversion to the long-wavelength part of the mid-IR spectral range. Judging by its absorption spectrum, however, at least by the available data on ZGP absorption [29,30], it is unlikely that OPCPA in this material can be pushed toward LWIR generation in the range of wavelengths beyond, roughly, 10 μm [see the blue line in Fig. 1(a)]. GaSe and AGSe crystals [30–35] seem to offer much more promise in this regard, as their transparency regions extend way beyond 10 μm [the green and purple lines in Fig. 1(a)].

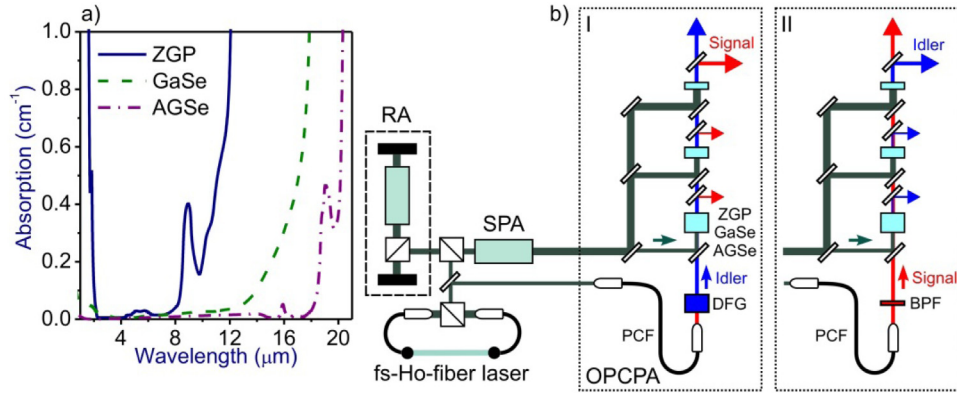


Fig. 1. (a) Absorption spectra of ZGP (blue line), GaSe (green line), and AGSe (purple line). (b) Diagram of broadband LWIR OPCPA seeded through the idler (scheme I) and signal (scheme II) fields: RA, regenerative amplifier of the pump source; SPA, single-pass amplifier of the pump source; PCF, photonic-crystal fiber; DFG, difference-frequency generation; ZGP/GaSe/AGSe, nonlinear crystals for broadband OPCPA in the LWIR range; BPF, band-pass filter.

OPCPA in ZGP can be phase-matched in the ooe polarization arrangement of the pump, signal, and idler waves. In this geometry, $\varepsilon_1(\theta, \omega) = n_o(\omega)$, $\varepsilon_2(\theta, \omega) = ((\sin \theta/n_e(\omega))^2 + (\cos \theta/n_o(\omega))^2)^{-1/2}$, $\varepsilon_3(\theta, \omega) = ((\sin \theta/n_e(\omega))^2 + (\cos \theta/n_o(\omega))^2)^{-1/2}$, and $d_{\text{eff}}(\theta) = d \sin(2\theta)$ with $d = 75.4$ pm/V, where $n_o(\omega)$ and $n_e(\omega)$ are the refractive indices of the ordinary and extraordinary waves with frequency ω . For the eoo arrangement of OPCPA in GaSe, we have $\varepsilon_1(\theta, \omega) = ((\sin \theta/n_e(\omega))^2 + (\cos \theta/n_o(\omega))^2)^{-1/2}$, $\varepsilon_2(\theta, \omega) = n_o(\omega)$, $\varepsilon_3(\theta, \omega) = n_o(\omega)$, and $d_{\text{eff}}(\theta) = -d \cos(\theta)$ with $d = -54$ pm/V. Finally, OPCPA in AGSe can be phase-matched in the eoo and eoe polarization arrangements, leading to $\varepsilon_1(\theta, \omega) = ((\sin \theta/n_e(\omega))^2 + (\cos \theta/n_o(\omega))^2)^{-1/2}$, $\varepsilon_2(\theta, \omega) = n_o(\omega)$, $\varepsilon_3(\theta, \omega) = n_o(\omega)$, and $d_{\text{eff}}(\theta) = d \sin(\theta)$ with $d = 33$ pm/V for the eoo geometry and $\varepsilon_1(\theta, \omega) = ((\sin \theta/n_e(\omega))^2 + (\cos \theta/n_o(\omega))^2)^{-1/2}$, $\varepsilon_2(\theta, \omega) = n_o(\omega)$, $\varepsilon_3(\theta, \omega) = ((\sin \theta/n_e(\omega))^2 + (\cos \theta/n_o(\omega))^2)^{-1/2}$, and $d_{\text{eff}}(\theta) = d \sin(2\theta)$ with $d = 33$ pm/V for the eoe arrangement.

We consider two schemes of broadband OPCPA in the LWIR range. In the first scheme [scheme I in Fig. 1(b)], the OPCPA process is seeded through the idler field. Such an approach requires an additional DFG stage to generate the seed field. As a compact, yet efficient solution, such a seed can be delivered, as elegantly shown in [15], via DFG in a CSP crystal seeded by a Tm, Ho fiber laser.

The second scheme of broadband OPCPA examined in this work [scheme II in Fig. 1(b)] is seeded through the signal field. This version of OPCPA does not require an additional stage for seed generation since a suitably red-shifted seed can be generated through a frequency broadening of the pump field in the bulk of mid-IR transparent solid or via soliton self-frequency shift in a properly designed optical fiber, e.g., a photonic-crystal fiber [36,37].

In both versions of LWIR OPCPA considered in this work, a holmium (Ho: YLF or Ho: YAG) laser is used as a source of pump pulses. When implemented in a scheme with regenerative and single-pass amplification, a Ho: YLF laser with a cw-Tm-fiber-laser pump has been shown [15,38] to enable the generation of 2.05- μm , 11-ps laser pulses with an energy up to 40 mJ at a pulse repetition rate of 100 Hz. In recent studies [39–43], kilohertz Ho: YAG and Ho: YLF laser sources capable of delivering 2.05 – 2.10- μm , 1 – 3-ps laser pulses with an energy of a few millijoules have been also demonstrated. Laser energies as high as 550 mJ have been achieved in the nanosecond output of holmium laser sources [44,45].

3. Model

Our analysis of broadband OPCPA in the LWIR range is based on a set of coupled equations [24] for the complex amplitudes $A_j(z, t)$ of the pump ($j = 1$), signal ($j = 2$), and idler ($j = 3$) waves with central frequencies ω_1 , ω_2 , and ω_3 , respectively, coupled by a $\omega_1 = \omega_2 + \omega_3$ parametric process,

$$\frac{\partial A_j(z, \omega)}{\partial z} = \left(i\tilde{D}_j - \frac{\alpha(\omega)}{2} \right) A_j(z, \omega) + \tilde{F} \left[\frac{i\omega_j \sigma_j}{c} P_j(z, t) \right] \quad (1)$$

Here, $A_j(z, \omega)$ is the Fourier transform of $A_j(z, t)$, z is the longitudinal coordinate, t is the time in the retarded frame for references, $\alpha(\omega)$ is the absorption, $\tilde{D}_j = k_j(\theta, \omega) - \partial k_1(\theta, \omega)/\partial \omega|_{\omega_1}$ is the dispersion operator, $k_j(\theta, \omega) = \omega_j \varepsilon_j(\theta, \omega)/c$, θ is the angle between the collinear wave vectors of the pump, signal, and idler fields and the optical axis of a crystal, $\sigma_j(\theta) = 2\kappa d_{\text{eff}}(\theta)(c\mu_0/(2n_1 n_2 n_3))^{1/2}$, n_j is the refractive index at the frequency of the j th field, κ is the mode-overlap integral, $P_1(z, t) = A_2(z, t)A_3(z, t)$, $P_2(z, t) = A_1(z, t)A_3^*(z, t)$, $P_3(z, t) = A_1(z, t)A_2^*(z, t)$, $d_{\text{eff}}(\theta)$ and $\varepsilon_j(\theta, \omega)$ are the factors whose specific form is determined by the polarization arrangement of the waves involved in OPCPA.

Written in the frequency domain, the set of Eqs. (1) extends the analysis of OPCPA beyond the standard framework of coupled equations for slowly varying field amplitudes [46], allowing the transient character of OPCPA of ultrashort pulses to be adequately described. Specifically, the dispersion operator \tilde{D}_j , appearing in Eq. (1), not only helps analyze phase-matching and group-delay effects, but also serves to include dispersion effects up to all the orders, which may play a significant role for field waveforms whose pulse widths approach the field cycle. Although nonlinear phase shifts and spatial self-action may become a significant factor, especially for high peak powers of the pump field, these effects are not included in Eq. (1). With such an approach we seek to identify, through a transparent physical analysis, the key limitations on short-pulse LWIR generation due to the dispersion of nonlinear materials that seem best suited for OPCPA in the LWIR range. While this approximation cannot reproduce all the details of spatiotemporal evolution of ultrashort pulses in nonlinear crystals, it will be shown to be instrumental in providing important physical insights into the OPCPA in the mid-IR and LWIR ranges, often enabling a quantitative description of this process within a broad range of parameter space, including an adequate explanation of milestone experiments on ultrashort-pulse generation near the long-wavelength edge of the mid-IR range [15].

In the case of continuous-wave fields, the set of Eqs. (1) allows a simple analytical solution [47]:

$$I_2 = I_{20} \left(1 + \gamma^2 / g^2 \sinh^2(gz) \right), \quad (2)$$

$$I_3 = I_{20} (\omega_3 / \omega_2) \left(\gamma^2 / g^2 \sinh^2(gz) \right), \quad (3)$$

where $\gamma^2 = 8\pi^2 c \mu_0 (\kappa d_{\text{eff}}(\theta))^2 I_{10} / (n_1 n_2 n_3 \lambda_2 \lambda_3)$, $g = (\gamma^2 - (\delta k/2)^2)^{1/2}$, I_{j0} is the input intensity of the j th field, and λ_j is the wavelength of the j th field.

For an OPCPA scheme seeded through the signal field, Eqs. (2) and (3) lead to the following solutions for the energies of the signal and idler fields:

$$W_2 = W_{20} (1 + \gamma^2 / g^2 \sin^2(gz)), \quad (4)$$

$$W_3 = W_{20} (\omega_3 / \omega_2) (\gamma^2 / g^2 \sin^2(gz)), \quad (5)$$

where W_{20} is the input energy of the signal field. A similar solution can be obtained for an OPCPA scheme seeded through the idler field.

Obviously, Eqs. (2) and (3) cannot describe any transient effects in short-pulse OPCPA or pump-depletion phenomena. However, solutions (4) and (5) are instructive, as they provide, as our analysis shows [dashed lines in Figs. 2–11], helpful approximate analytical expressions for the energies of the signal and idler fields in the regime of undepleted pump.

In the opposite limiting case of complete pump depletion, the Manley–Rowe relations [48] applied to pulses whose pulse widths remain almost constant through the entire OPCPA process yield

$$W_2 = W_{10} \tau_2 \omega_2 n_1 / (\tau_1 \omega_1 n_2), \quad (6)$$

$$W_3 = W_{10} \tau_3 \omega_3 n_1 / (\tau_1 \omega_1 n_3), \quad (7)$$

where τ_j are the pulse widths and the seed energy in either the signal or the idler input field is assumed to be much lower than the pump energy.

As our analysis presented below shows, Eqs. (6) and (7) provide accurate predictions for the asymptotic upper-bound limit for the signal and idler energies [dotted lines in Figs. 2–11], serving as a guide that helps choose the crystal thickness for each OPCPA stage.

4. Results and discussion

4.1. Model verification

Before proceeding with the analysis of LWIR generation, we verify our model by examining an idler-seeded OPCPA in ZGP crystals as implemented in recent experiments by Sanchez et al. [15], yielding a short-pulse idler output on the long-wavelength side of the mid-IR range. In Fig. 2, we present the results of extended coupled-wave analysis of a collinear ope OPCPA in three ZGP crystals pumped by 10-ps, 2.04- μm laser pulses and seeded by negatively chirped 3.3-ps pulses with a central wavelength of 7.0 μm and a spectrum corresponding to a transform-limited pulse width of 100 fs. Figure 2(a) displays a map of the OPCPA coherence length $l_c = \pi/|\delta k|$, where $\delta k = k_1 - k_2 - k_3$ is the wave-vector mismatch, calculated as a function of the idler wavelength and the angle θ . All the three ZGP crystals are oriented at an angle $\theta = 52.9^\circ$ in the considered OPCPA scheme to phase match the parametric amplification of the 7.0- μm seed. The energy of 2.04- μm laser pulses used to pump the three OPCPA stages are set equal to 0.2, 4, and 10 mJ. In the first OPCPA stage, the idler field grows from the seed level [80 pJ, the dotted line in Fig. 2(b)] up to approximately 10 μJ . In the second and third stages [Figs. 2(c), 2(d)], the idler field undergoes further parametric amplification until it reaches a level of saturation at approximately 0.55 mJ at the output of the third ZGP crystal. The spectrum of the idler output of the third OPCPA stage [Fig. 2(e)] corresponds to a Fourier-transform pulse width of about 150 fs. The results of these simulations agree reasonably well with recent experimental studies by Sanchez et al. [15], showing that, although our model does not include the nonlinear phase shift and spatial self-action, it still provides an adequate quantitative description of the key tendencies in short-pulse OPCPA near the long-wavelength edge of the mid-IR range.

4.2. Idler-seeded OPCPA in the LWIR range

With the predictive power of our model confirmed by comparison with recent experiments performed in the long-wavelength region of the mid-IR spectral range, we are now in a position to demonstrate that broadband OPCPA is ideally suited to deliver a high-peak-power short-pulse output in the LWIR spectra range. To this end, we examine broadband OPCPA in nonlinear crystals transparent through most of or through the entire LWIR range, such as GaSe and AGSe [green and purple curves in Fig. 1(a)].

An idler output with even longer wavelengths can be generated through broadband OPCPA in AGSe crystals [Figs. 4 and 5]. The coherence length maps for eoo and eoe OPCPA with a 2.04- μm pump in this crystal is shown in Figs. 4(b) and 5(b). Sequential parametric amplification of 13- and 16- μm , 3.3-ps seed in three AGSe crystals oriented at, respectively, $\theta = 43.6^\circ$ and 48.8° yields, through eoo and eoe parametric interaction [Figs. 4(b)–4(d), 5(b)–5(d)], a 0.67- and 0.61-mJ idler-wave output at 13 and 16 μm [Figs. 4(b), 5(b)]. The spectrum of this idler-wave OPCPA output supports transform-limited pulse widths of 100 fs at 13 μm and at 16 μm , corresponding to 2.3 and 1.9 field cycles at these central wavelengths.

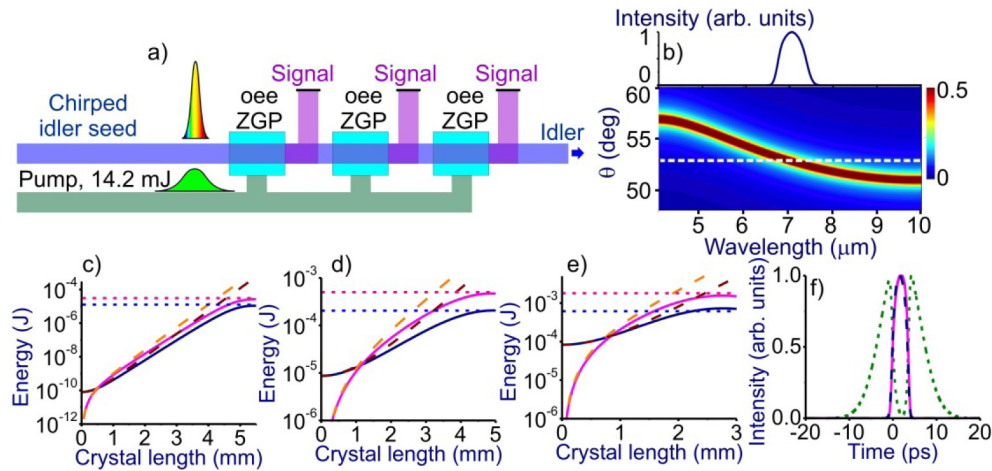


Fig. 2. Idler-seeded collinear ooe OPCPA in a cascade of ZGP crystals with a 14.2-mJ pump: (a) three $\theta = 52.9^\circ$ ZGP crystals pumped by 10-ps, 2.04- μm laser pulses with energies of 0.2, 4, and 10 mJ, respectively, and seeded by negatively chirped 3.3-ps, 80-pJ pulses with a central wavelength of 7.0 μm and a spectrum corresponding to a transform-limited pulse width of 100 fs, (b) the coherence length for this OPCPA process as a function of the idler wavelength and the angle θ with the spectrum of the idler output of the three-stage OPCPA shown on top, (c – e) the energies of the signal (red) and idler (blue) fields as functions of the propagation path inside the first (c), second (d), and third (e) ZGP crystals, and (f) temporal envelopes of the pump (green dots), signal (red solid), and idler (blue dashes) pulses at the output of the three-stage OPCPA. Also shown are the solutions (4) and (5) (dashed lines), the Manley–Rowe asymptotic values of the signal and idler energies, as defined by Eqs. (6) and (7) (dotted lines), and the seed energy (dash–dotted line).

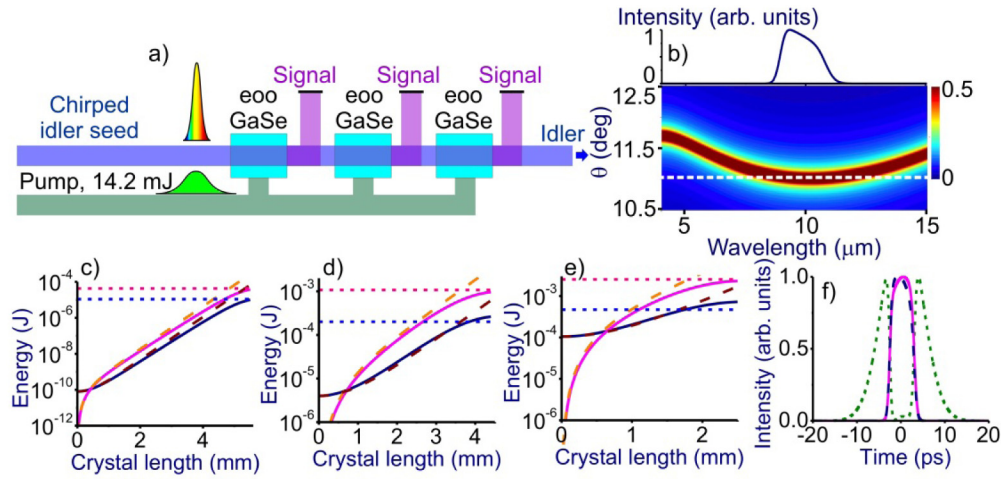


Fig. 3. Idler-seeded collinear eoo OPCPA in a cascade of GaSe crystals with a 14.2-mJ pump: (a) three $\theta = 11^\circ$ GaSe crystals pumped by 10-ps, 2.04- μm laser pulses with energies of 0.2, 4, and 10 mJ, respectively, and seeded by negatively chirped 3.3-ps, 80-pJ pulses with a central wavelength of 10 μm and a spectrum corresponding to a transform-limited pulse width of 100 fs, (b) the coherence length for this OPCPA process as a function of the idler wavelength and the angle θ with the spectrum of the idler output of the three-stage OPCPA shown on top, (c – e) the energies of the signal (red) and idler (blue) fields as functions of the propagation path inside the first (c), second (d), and third (e) GaSe crystals; (f) temporal envelopes of the pump (green dots), signal (red solid), and idler (blue dashes) pulses at the output of the three-stage OPCPA. Also shown are the solutions (4) and (5) (dashed lines), the Manley–Rowe upper-bound values of the signal and idler energies, as defined by Eqs. (6) and (7) (dotted lines), and the seed energy (dash-dotted line).

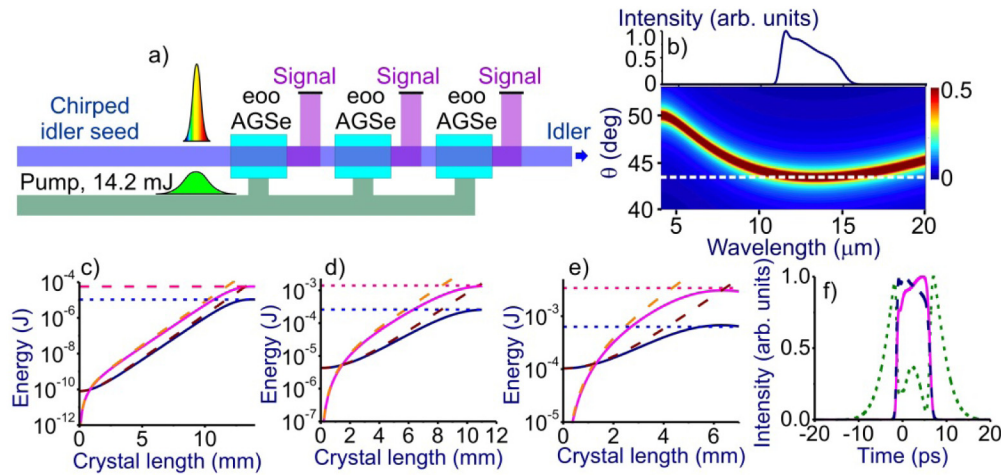


Fig. 4. Idler-seeded collinear eoo OPCPA in a cascade of AGSe crystals with a 14.2-mJ pump: (a) three 43.6° AGSe crystals pumped by 10-ps, 2.04- μm laser pulses with energies of 0.2, 4, and 10 mJ, respectively, and seeded by negatively chirped 3.3-ps, 80-pJ pulses with a central wavelength of 13 μm and a spectrum corresponding to a transform-limited pulse width of 100 fs, (b) the coherence length for this OPCPA process as a function of the idler wavelength and the angle θ with the spectrum of the idler output of the three-stage OPCPA shown on top, (c – e) the energies of the signal (red) and idler (blue) fields as functions of the propagation path inside the first (c), second (d), and third (e) AGSe crystals, and (f) temporal envelopes of the pump (green dots), signal (red solid), and idler (blue dashes) pulses at the output of the three-stage OPCPA. Also shown are the solutions (4) and (5) (dashed lines), the Manley–Rowe upper-bound values of the signal and idler energies, as defined by Eqs. (6) and (7) (dotted lines), and the seed energy (dash-dotted line).

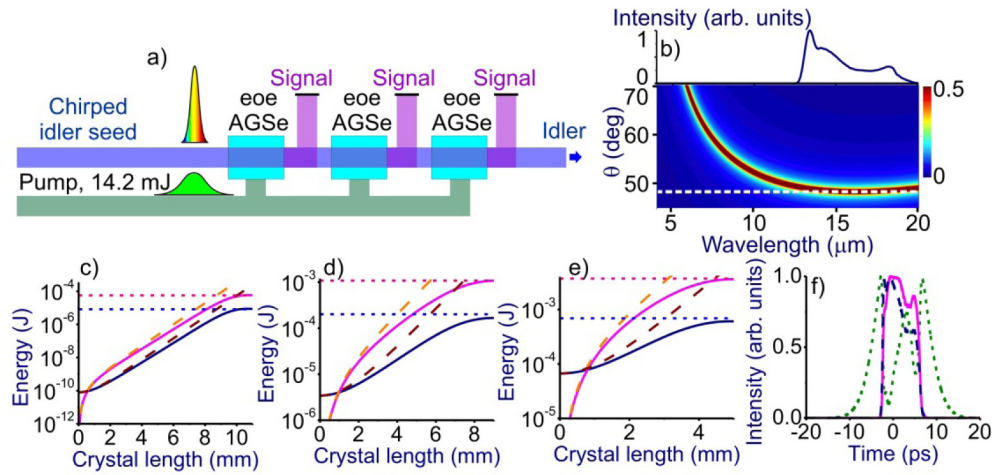


Fig. 5. Idler-seeded collinear eoe OPCPA in a cascade of AGSe crystals with a 14.2-mJ pump: (a) three 48.3° AGSe crystals pumped by 10-ps, $2.04\text{-}\mu\text{m}$ laser pulses with energies of 0.2, 4, and 10 mJ, respectively, and seeded by negatively chirped 3.3-ps, 80-pJ pulses with a central wavelength of $16\text{ }\mu\text{m}$ and a spectrum corresponding to a transform-limited pulse width of 100 fs, (b) the coherence length for this OPCPA process as a function of the idler wavelength and the angle θ with the spectrum of the idler output of the three-stage OPCPA shown on top, (c – e) the energies of the signal (red) and idler (blue) fields as functions of the propagation path inside the first (c), second (d), and third (e) AGSe crystals, and (f) temporal envelopes of the pump (green dots), signal (red solid), and idler (blue dashes) pulses at the output of the three-stage OPCPA. Also shown are the solutions (4) and (5) (dashed lines), the Manley–Rowe upper-bound values of the signal and idler energies, as defined by Eqs. (6) and (7) (dotted lines), and the seed energy (dash-dotted line).

4.3. Signal-seeded OPCPA in the LWIR range

In Figs. 6 and 7, we illustrate the performance attainable with the second OPCPA approach, where the OPCPA is seeded through the signal rather than the idler input, thus allowing a radical simplification of the OPCPA apparatus at the expense, perhaps, of CEP stability. For the convenience of comparison, the input pulse width of the signal seed in calculations presented in Figs. 6 and 7 (3.3 ps) is chosen equal to the input seed pulse width in calculations for the idler-seeded OPCPA in Figs. 3–5. However, since the seed pulses on both OPCPA schemes are chirped in such a way that their transform-limited pulse width is equal to 100 fs, dispersion of a nonlinear crystal leads to pulse stretching. Because dispersion at the idler wavelength noticeably differs from the dispersion at the signal wavelengths, the amplified output pulse width in the idler-seeded OPCPA [Figs. 3–5] is different from that in OPCPA with a signal seed [Figs. 6, 7].

When seeded with negatively chirped 3.3-ps pulses with a central wavelength of $2.38\text{ }\mu\text{m}$, collinear eoe OPCPA in three AGSe crystals [Figs. 6(a)–6(e)], all tilted at $\theta = 43.6^\circ$, yields a broadband output with a spectrum centered at $\lambda_3 \approx 13.5\text{ }\mu\text{m}$ [Fig. 6(b)]. The energy of this LWIR signal at the output of the third crystal [Fig. 6(e)] is about 0.44 mJ. The transform-limited pulse width of this signal is about 100 fs, which corresponds to 2.2 field cycles. An eoe OPCPA process in three AGSe crystals with $\theta = 48.8^\circ$ seeded with negatively chirped 3.3-ps pulses at $2.34\text{ }\mu\text{m}$ [Figs. 7(a)–7(e)], on the other hand, delivers an idler-wave output centered at $\lambda_3 \approx 16\text{ }\mu\text{m}$ [Fig. 7(b)] with an energy of about 0.28 mJ [Fig. 7(e)] and a spectrum corresponding to a transform-limited pulse width of 100 fs [Fig. 7(b)], which corresponds to 1.9 field cycles.

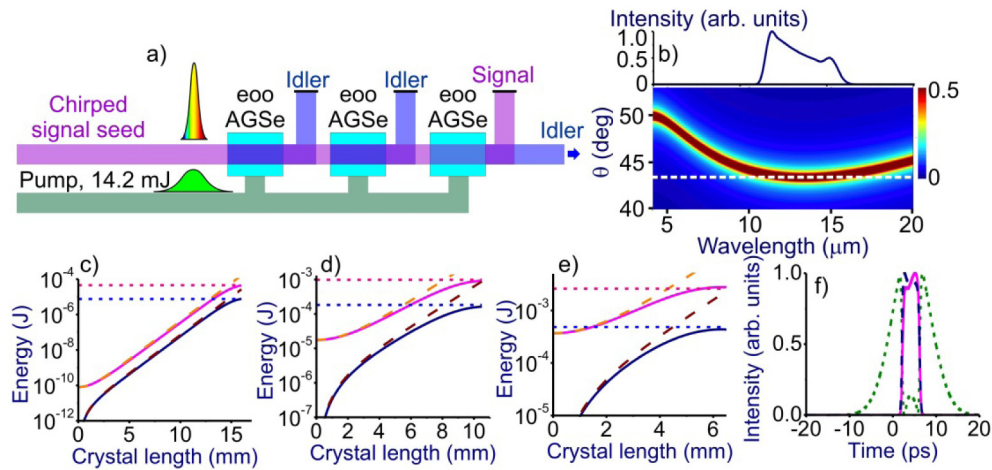


Fig. 6. Signal-seeded collinear eoo OPCPA in a cascade of AGSe crystals with a 14.2-mJ pump: (a) three 43.6° AGSe crystals pumped by 10-ps, $2.04\text{-}\mu\text{m}$ laser pulses with energies of 0.2, 4, and 10 mJ, respectively, and seeded by negatively chirped 3.3-ps, 80-pJ pulses with a central wavelength of $2.38\text{ }\mu\text{m}$ and a spectrum corresponding to a transform-limited pulse width of 100 fs, (b) the coherence length for this OPCPA process as a function of the idler wavelength and the angle θ with the spectrum of the idler output of the three-stage OPCPA shown on top; (c – e) the energies of the signal (red) and idler (blue) fields as functions of the propagation path inside the first (c), second (d), and third (e) AGSe crystals, and (f) temporal envelopes of the pump (green dots), signal (red solid), and idler (blue dashes) pulses at the output of the three-stage OPCPA. Also shown are the solutions (4) and (5) (dashed lines), the Manley–Rowe upper-bound values of the signal and idler energies, as defined by Eqs. (6) and (7) (dotted lines), and the seed energy (dash-dotted line).

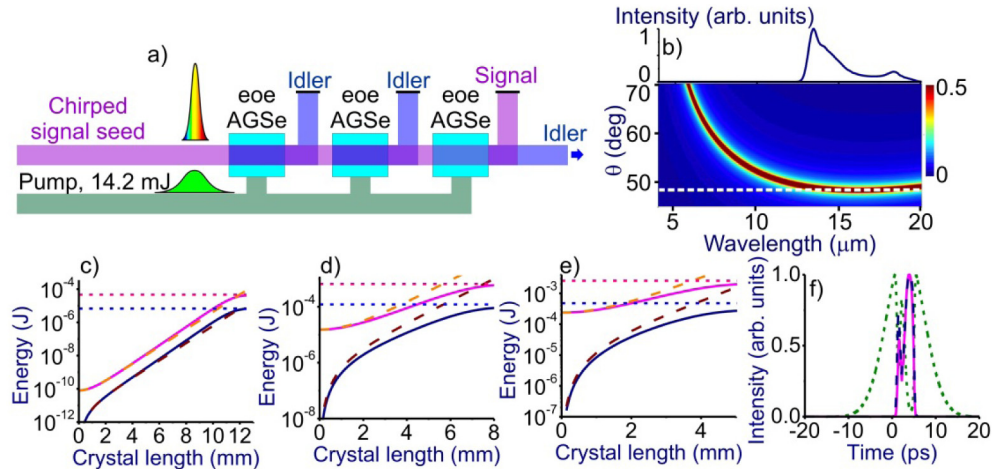


Fig. 7. Signal-seeded collinear eoe OPCPA in a cascade of AGSe crystals with a 14.2-mJ pump: (a) three 48.3° AGSe crystals pumped by 10-ps, $2.04\text{-}\mu\text{m}$ laser pulses with energies of 0.2, 4, and 10 mJ, respectively, and seeded by negatively chirped 3.3-ps, 80-pJ pulses with a central wavelength of $2.34\text{ }\mu\text{m}$ and a spectrum corresponding to a transform-limited pulse width of 100 fs, (b) the coherence length for this OPCPA process as a function of the idler wavelength and the angle θ with the spectrum of the idler output of the three-stage OPCPA shown on top; (c – e) the energies of the signal (red) and idler (blue) fields as functions of the propagation path inside the first (c), second (d), and third (e) AGSe crystals, and (f) temporal envelopes of the pump (green dots), signal (red solid), and idler (blue dashes) pulses at the output of the three-stage OPCPA. Also shown are the solutions (4) and (5) (dashed lines), the Manley–Rowe upper-bound values of the signal and idler energies, as defined by Eqs. (6) and (7) (dotted lines), and the seed energy (dash-dotted line).

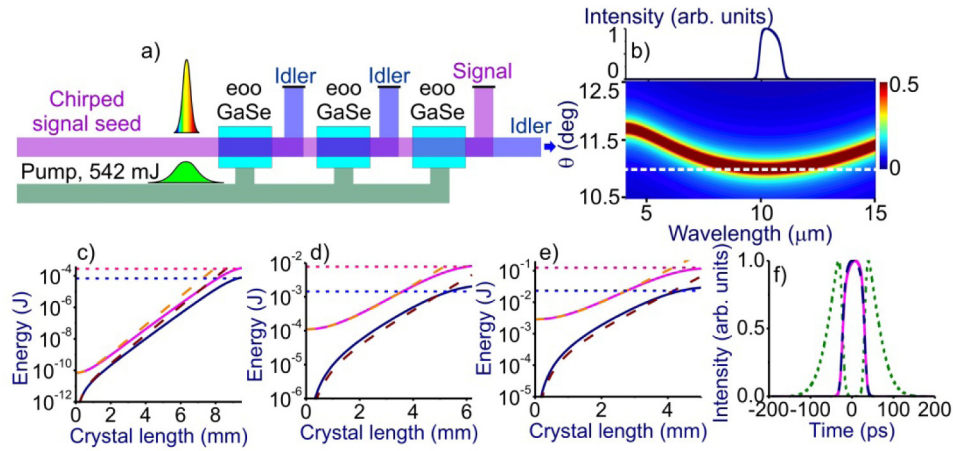


Fig. 8. Signal-seeded collinear eoo OPCPA in a cascade of GaSe crystals with a 542-mJ pump: (a) three $\theta = 11^\circ$ GaSe crystals pumped by 10-ps, 2.04- μm laser pulses with energies of 2, 40, and 500 mJ, respectively, and seeded by negatively chirped 5.5-ps, 80-pJ pulses with a central wavelength of 2.54 μm and a spectrum corresponding to a transform-limited pulse width of 200 fs, (b) the coherence length for this OPCPA process as a function of the idler wavelength and the angle θ with the spectrum of the idler output of the three-stage OPCPA shown on top; (c – e) the energies of the signal (red) and idler (blue) fields as functions of the propagation path inside the first (c), second (d), and third (e) AGSe crystals, and (f) temporal envelopes of the pump (green dots), signal (red solid), and idler (blue dashes) pulses at the output of the three-stage OPCPA. Also shown are the solutions (4) and (5) (dashed lines), the Manley–Rowe upper-bound values of the signal and idler energies, as defined by Eqs. (6) and (7) (dotted lines), and the seed energy (dash-dotted line).

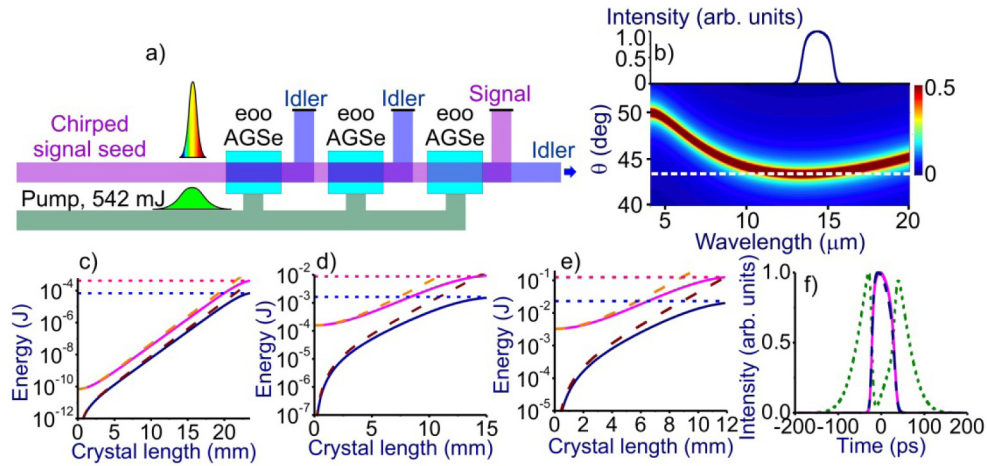


Fig. 9. Signal-seeded collinear eoo OPCPA in a cascade of AGSe crystals with a 542-mJ pump: (a) three 43.6° AGSe crystals pumped by 10-ps, 2.04- μm laser pulses with energies of 2, 40, and 500 mJ, respectively, and seeded by negatively chirped 5.5-ps, 80-pJ pulses with a central wavelength of 2.38 μm and a spectrum corresponding to a transform-limited pulse width of 200 fs, (b) the coherence length for this OPCPA process as a function of the idler wavelength and the angle θ with the spectrum of the idler output of the three-stage OPCPA shown on top; (c – e) the energies of the signal (red) and idler (blue) fields as functions of the propagation path inside the first (c), second (d), and third (e) AGSe crystals, and (f) temporal envelopes of the pump (green dots), signal (red solid), and idler (blue dashes) pulses at the output of the three-stage OPCPA. Also shown are the solutions (4) and (5) (dashed lines), the Manley–Rowe upper-bound values of the signal and idler energies, as defined by Eqs. (6) and (7) (dotted lines), and the seed energy (dash-dotted line).

4.4. LWIR OPCPA with a high-peak-power pump

To understand the approaches whereby OPCPA technologies enabling the generation of ultrashort high-peak-power pulses in the mid-IR [5–8] could be extended to the LWIR range, we consider broadband OPCPA in ZGP, GaSe, and AGSe crystals pumped by 2.04- μm laser pulses with an energy up to 542 mJ. Such a level of pulse energy is attainable with Ho: YLF [44], as well as with Cr, Tm, Ho: YAG [45] lasers, albeit currently not in the picosecond, but in the nanosecond Q-switching operation mode. With OPCPA solutions for high-peak-power short-pulse generation in the mid-IR [5–8] used as a guidance for minimizing unwanted nonlinear phase shifts and spatial self-action, we set the pump pulse width in our LWIR OPCPA scheme at 100 ps. With a seed delivered in negatively chirped 42-ps pulses at 2.73 μm , an OPCPA system consisting of three ZGP crystals oriented at $\theta = 52^\circ$ can then deliver an LWIR output with a central wavelength $\lambda_3 \approx 8.2 \mu\text{m}$ and an output energy of 36.9 mJ, compressible to a transform-limited pulse width of 260 fs (Table 1). An OPCPA based on three $\theta = 11^\circ$ GaSe crystals seeded by negatively chirped 42-ps pulses at 2.54 μm [Figs. 8(a)–8(e)], on the other hand, enables the generation of a 28.9-mJ idler output centered at $\lambda_3 \approx 10.3 \mu\text{m}$ [Fig. 8(b)], supporting a transform-limited pulse width of 255 fs (7.4 field cycles). Finally, OPCPA using three AGSe crystals [Figs. 9,10] can deliver 20.1-mJ LWIR pulses as its idler output centered at $\lambda_3 \approx 14.3 \mu\text{m}$ in the case of eoo parametric amplification with $\theta = 43.6^\circ$ and a seed at 2.38 μm [Figs. 9(a)–9(f)] and 21-mJ LWIR pulses as its idler output centered at $\lambda_3 \approx 16 \mu\text{m}$ in the eoe OPCPA geometry with $\theta = 48.3^\circ$ and a seed at 2.34 μm [Figs. 10(a)–10(f)]. In both regimes, the LWIR OPCPA output is compressible to a transform-limited pulse width of 260 fs. The LWIR OPCPA output energies in both schemes are seen to be less than 10% below the fundamental limit dictated by the Manley–Rowe relations [cf. the solid and dotted lines in Figs. 9(c)–9(e), 10(c)–10(e)]. To reduce the risk of laser damage, the energy fluence in all the calculations performed for OPCPA with a 542-mJ pump was kept below 2.4 J/cm².

5. OPCPA in the LWIR range: examining options

We are now in a position to compare the performance of various OPCPA schemes for the generation of ultrashort pulses in the LWIR range. As can be seen from the absorption spectra presented in Fig. 1(a), the ZGP crystal, despite its excellent performance at the long-wavelength edge of the mid-IR range [15], is not suitable for LWIR generation with $\lambda > 10 \mu\text{m}$ as its loss rapidly grows in this wavelength range [blue solid line in Fig. 1(a)]. The AGSe crystal, on the other hand, is an especially attractive option for short-pulse LWIR generation as this material is transparent within the entire LWIR range and even beyond this range, up to wavelengths as long as 20 μm [purple dash-dotted line in Fig. 1(a)]. The damage thresholds for all the three materials are comparable, falling in the range of a few J/cm² for ~100-ps pulses in the 2 – 3- μm wavelength region [27,30,49–51].

Typical parameters of long-wavelength OPCPA systems attainable with ZGP, GaSe, and AGSe crystals are summarized in Table 1. As a general tendency, the ZGP and GaSe crystals provide the highest gain in the OPCPA scheme, allowing the thicknesses of nonlinear crystals in all the OPCPA stages to be reduced, thus minimizing high-order dispersion effects and nonlinear phase shifts. However, in addition to the limited transmission window in the LWIR range [solid line in Fig. 1(a)], ZGP crystal suffers from a narrow OPCPA gain band, as the dispersion of ZGP supports broadband phase matching only near the edge of its transparency region [the flat region of the phase-matching map in Fig. 2(b)]. The GaSe crystal, as can be seen from Fig. 3 and Table 1, is well-suited for the generation of ~100-fs pulses around 10 μm [Fig. 3]. The AGSe crystal, on the other hand, is not only transparent within the entire LWIR range [purple line in Fig. 1(a)], but also supports the broadest phase matching among all three materials considered here [Figs. 4(b)–7(b), 9(b), 10(b)]. As a result, this crystal enables the generation of pulses as short as 100 fs with a central wavelength as long as 16 μm

[Figs. 5, 10]. Moreover, different types of phase matching supported by AGSe (Table 1) provides additional wavelength tunability of the LWIR OPCPA output. In particular, OPCPA in AGSe with eoo and eoe phase matching can deliver a short-pulse LWIR output with a pulse width of 100 fs centered at 13 μm [Fig. 4] and 16 μm [Fig. 5], respectively.

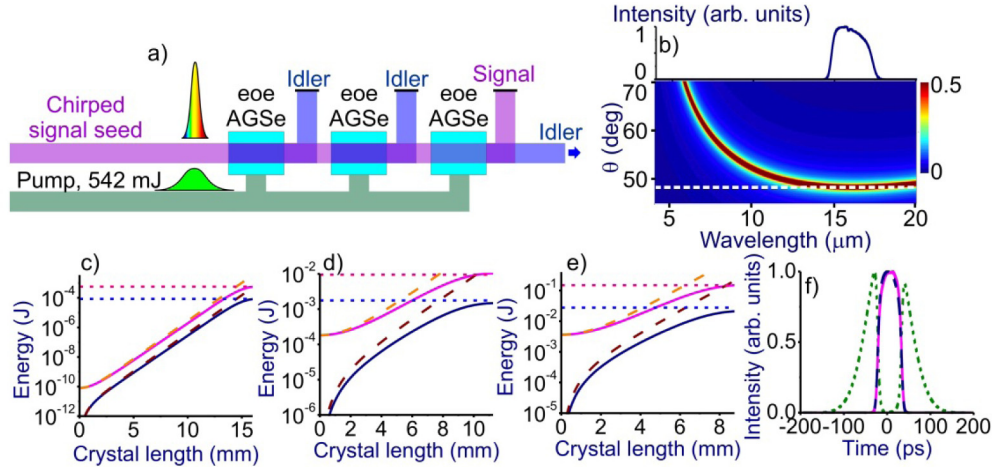


Fig. 10. Signal-seeded collinear eoe OPCPA in a cascade of AGSe crystals with a 542-mJ pump: (a) three 48.3° AGSe crystals pumped by 10-ps, $2.04\text{-}\mu\text{m}$ laser pulses with energies of 2, 40, and 500 mJ, respectively, and seeded by negatively chirped 5.5-ps, 80-pJ pulses with a central wavelength of $2.34\text{ }\mu\text{m}$ and a spectrum corresponding to a transform-limited pulse width of 200 fs, (b) the coherence length for this OPCPA process as a function of the idler wavelength and the angle θ with the spectrum of the idler output of the three-stage OPCPA shown on top; (c – e) the energies of the signal (red) and idler (blue) fields as functions of the propagation path inside the first (c), second (d), and third (e) AGSe crystals, and (f) temporal envelopes of the pump (green dots), signal (red solid), and idler (blue dashes) pulses at the output of the three-stage OPCPA. Also shown are the solutions (4) and (5) (dashed lines), the Manley–Rowe upper-bound values of the signal and idler energies, as defined by Eqs. (6) and (7) (dotted lines), and the seed energy (dash-dotted line).

Table 1. Parameters of short-pulse OPCPA using ZGP, GaSe, and AGSe crystals

Crystal	Seed	PM	λ , μm	l_1, l_2, l_3 , mm	W_1, W_2, W_3 , mJ	τ_{out} , ps	τ_0 , fs	τ_0/T_0	W_{out} , mJ
ZGP	idler	oee	7.0	5.5, 5, 2.7	0.2, 4, 10	3.5	150	6.4	0.55
	signal	oee	8.2	6.5, 4.3, 3	2, 40, 500	53.7	260	9.5	36.9
GaSe	idler	eoo	10.0	5.5, 4.4, 2.5	0.2, 4, 10	5.4	105	3.2	0.73
	signal	eoo	10.3	9.5, 6.2, 5	2, 40, 500	52.3	255	7.4	28.9
AGSe	idler	eoo	13.0	14, 11, 7	0.2, 4, 10	7.5	100	2.3	0.67
		eoe	16.0	11, 9, 5	0.2, 4, 10	7.9	100	1.88	0.61
	signal	eoo	13.5	16, 10.5, 6.5	0.2, 4, 10	3.9	100	2.2	0.44
		eoe	16.0	12.5, 8, 5.2	0.2, 4, 10	3.4	100	1.88	0.28
		eoo	14.3	24, 15, 11.9	2, 40, 500	50.4	260	5.5	20.1
		eoe	16.0	16, 11.3, 8.8	2, 40, 500	53	260	4.9	21

Notation: PM, phase-matching type; λ , output wavelength; l_1, l_2, l_3 , lengths of crystals in the first, second, and third OPCPA stages; W_1, W_2, W_3 , pump energies in the first, second, and third OPCPA stages; τ_{out} , output pulse width; τ_0 , transform-limited pulse width supported by the entire OPCPA output spectrum; T_0 , field cycle duration; W_{out} , output energy.

Idler- and signal-seeded OPCPA schemes provide comparable OPCPA gain bands [Figs. 3(b)–7(b)], limited by phase-matching bandwidths, both enabling the generation of ~ 100 -fs LWIR pulses [Figs. 3(b)–7(b)]. However, the efficiency of idler-wave parametric amplification is generally much higher than the efficiency of signal-seeded OPCPA. This is largely due to two factors. First, due to the Manley–Rowe-type photon-number conservation [see Eqs. (6), (7)], parametric amplification of an idler wave is generally more efficient than the parametric amplification of a signal field. Second, the dispersion-induced stretching of the idler pulse in our OPCPA scheme is stronger than the stretching of the signal pulse, which reduces the group delay and spatial walk-off of these pulses relative to the pump. As a result, the output pulse in idler-seeded OPCPA is noticeably longer than the input seed pulse [Figs. 3(f), 4(f), 5(f)]. However, with a proper optimization of the OPCPA scheme, this dispersion-induced pulse stretching does not reduce the OPCPA gain bandwidth. Specifically, the output spectrum of the idler-seeded OPCPA in Figs. 4(b), 5(b) is compressible to a transform-limited pulse width as short as 100 fs.

As an important advantage, OPCPA with a signal seed does not require an additional stage for seed generation since a suitably red-shifted seed can be generated through a frequency broadening of the pump field in the bulk of mid-IR transparent solid or via soliton self-frequency shift in a properly designed optical fiber, e.g., a photonic-crystal fiber [36,37]. However, as a reward for an additional complexity of idler-seeded OPCPA, the carrier-envelope phase (CEP) of the parametrically amplified field in this scheme is intrinsically stable.

Analysis of OPCPA pumped with high-peak-power pulses shows that, unless nonlinear phase shifts and spatial self-action effects start to play a noticeable role, OPCPA efficiencies comparable to those attainable in the low-power regime can be achieved for short-pulse OPCPA output energies as high as 20 – 40 mJ [Table 1, Figs. 8–10]. However, to provide this level of OPCPA efficiencies, we had to take seed pulses with a smaller bandwidth, thus limiting the spectral bandwidth and, hence the minimum pulse width of the OPCPA output. In this regime, ultrashort pulses with a peak power up to 100 – 180 GW could be generated within a broad wavelength range from approximately 8 to 16 μm [Figs. 8–10 and Table 1].

6. Conclusion

To summarize, our coupled-wave analysis of OPCPA in LWIR-transparent nonlinear crystals reveals regimes whereby high-peak-power few-cycle pulses can be generated in the long-wavelength infrared (LWIR) spectral range. Broadband OPCPA in suitable nonlinear crystals pumped at around 2 μm and seeded either through the signal or the idler input is shown to enable the generation of high-power field waveforms with pulse widths shorter than two field cycles within the entire LWIR range.

Funding

Russian Foundation for Basic Research (project nos. 14-29-07182, 16-32-60164, 15-32-20713 and 16-02-00843); Welch Foundation (grant no. A-1801); Russian Science Foundation (14-12-00772); ONR (Award no. 00014-16-1-2578).